AGU PUBLICATIONS

Water Resources Research

RESEARCH ARTICLE
10.1002/2017WR020515

Key Points:
- Thermodynamics of altiplanic wetlands requires heat exchanges between water and sediments
- Water temperature decomposition into Fourier series
- Use of the solution for the second problem of Stokes for sediment temperature

Correspondence to:
A. de la Fuente,
aldelafu@ing.uchile.cl

Citation:
de la Fuente, A., and C. Meruane (2017), Spectral model for long-term computation of thermodynamics and potential evaporation in shallow wetlands, *Water Resour. Res.*, *53*, 7696–7715, doi:10.1002/2017WR020515.

Received 2 FEB 2017
Accepted 29 JUL 2017
Accepted article online 3 AUG 2017
Published online 4 SEP 2017

Spectral model for long-term computation of thermodynamics and potential evaporation in shallow wetlands

Alberto de la Fuente[1] and Carolina Meruane[1,2]

[1]Departamento de Ingeniería Civil, Universidad de Chile, Santiago, Chile, [2]Modelación Ambiental SpA, Santiago, Chile

Abstract Altiplanic wetlands are unique ecosystems located in the elevated plateaus of Chile, Argentina, Peru, and Bolivia. These ecosystems are under threat due to changes in land use, groundwater extractions, and climate change that will modify the water balance through changes in precipitation and evaporation rates. Long-term prediction of the fate of aquatic ecosystems imposes computational constraints that make finding a solution impossible in some cases. In this article, we present a spectral model for long-term simulations of the thermodynamics of shallow wetlands in the limit case when the water depth tends to zero. This spectral model solves for water and sediment temperature, as well as heat, momentum, and mass exchanged with the atmosphere. The parameters of the model (water depth, thermal properties of the sediments, and surface albedo) and the atmospheric downscaling were calibrated using the MODIS product of the land surface temperature. Moreover, the performance of the daily evaporation rates predicted by the model was evaluated against daily pan evaporation data measured between 1964 and 2012. The spectral model was able to correctly represent both seasonal fluctuation and climatic trends observed in daily evaporation rates. It is concluded that the spectral model presented in this article is a suitable tool for assessing the global climate change effects on shallow wetlands whose thermodynamics is forced by heat exchanges with the atmosphere and modulated by the heat-reservoir role of the sediments.

1. Introduction

The climatic and geological conditions of the Andean mountains have generated numerous wetland ecosystems on the elevated plateaus of Chile, Argentina, Peru, and Bolivia. These wetlands are the result of groundwater upwelling that flows to a terminal shallow wetland located at the central depression of a closed basin [*Risacher et al.*, 2003; *Cabrol et al.*, 2009; *de la Fuente and Niño*, 2010]. These systems are hydrologically closed, as the water that precipitates in the basin is completely evaporated from the terminal shallow wetland, thus evapoconcentrating the salts and reaching values as high as 150 g L^{-1}, which is why these shallow wetlands are named Salars [*Dorador et al.*, 2009; *de la Fuente and Niño*, 2010]. The desert climate and high altitude of these systems (higher than 3000 m above sea level) impose extreme environmental conditions on the ecosystems, such as low oxygen in the atmosphere, high levels of ultraviolet radiation, high daily temperature ranges, and hypersaline waters [*de la Fuente*, 2014a; *Hernández et al.*, 2016], thus resembling many aspects of the environment in which life originally developed on Earth [*Belluscio*, 2009]. Furthermore, the water temperature varies by 20–30°C in a day [*de la Fuente and Niño*, 2010; *de la Fuente*, 2014a].

Most of the uniqueness of these systems is explained by the fact that their size and water salinity are controlled by the balance between precipitation and evaporation rates [*de la Fuente and Niño*, 2010]. Consequently, these systems are particularly vulnerable to changes in land use, groundwater extractions, and climate change [*Junk et al.*, 2013] that will modify the water content and air temperature of the atmosphere, thus modifying the water balance through changes in precipitation and evaporation rates, retention time, and biogeochemical cycles. Monitoring and understanding the long-term effects of climate change on Salars should be a pressing concern of local governments, as these systems, similar to lakes, should be considered as sentinels of climate change [*Adrian et al.*, 2009; *Williamson et al.*, 2009].

To assess the impact of climate change on Salars, it is first necessary to simulate the thermodynamics of the system in response to the long-term changes in meteorological forcing of wind speed, air temperature, specific humidity, atmospheric pressure, solar radiation, and cloud cover. In particular, based on the features of

Salars, the thermodynamic model must account for the heat-reservoir function of the sediments that retain heat during the day and release it during the night [*de la Fuente and Niño*, 2010; *de la Fuente*, 2014a]. The meteorological forcing variables will change over time in response to greenhouse gas concentrations in the atmosphere, and to address the uncertainty in their evolution, four representative concentration pathways (RCPs) were defined by the Coupled Model Intercomparison Project Phase 5 [*Moss et al*., 2010; *van Vuuren et al*., 2011].

We identify three aspects that should be considered for conducting long-term thermodynamics simulations of altiplanic wetlands: (i) in the same way than for other shallow systems [*Piccolo*, 2009], heat exchanges with the sediments should be considered to properly represent heat budgets of shallow wetlands [*de la Fuente and Niño*, 2010; *de la Fuente*, 2014a]; (ii) the stable transition is required for the limit case when the water depth (h) goes to zero, in which the heat exchanges with the sediments balance heat exchanges with the atmosphere; and (iii) an efficient numerical algorithm is needed for the long-term simulations. Although previous researches have successfully addressed some of these three requirements, thus far, models or algorithms able to simultaneously address all of these requirements are not yet available. First of all, previous research has proposed numerical models that explicitly include ground heat exchanges for solving land surface temperature [*Liang et al*., 1999; *Sheng et al*., 2009]; however, these models do not consider the existence of a shallow water column on the top of the surface. In a similar way, *Confalonieri et al*. [2005] proposed an efficient algorithm for computing water temperature in flooded rice fields based on an empirical equation for computing the heat stored in the water column whose depth varies between 2 and 10 cm; however, these models do not consider the limit case when water depth goes to zero. Furthermore, heat exchanges with the sediments for computing water temperature have been efficiently included in models such as FLake [*Golosov and Kirillin*, 2010]; however, these models are primarily designed to deal with stratification and vertical mixing, which are not relevant processes in a 0–15 cm-deep water column, and they were not specifically designed to address the transition when $h \rightarrow 0$, where the numerical model is not able to provide a stable solution. Similar situation can be observed in, for example, *Smesrud et al*. [2014] who solved horizontal distribution of water temperature including longitudinal advection and dispersion. More sophisticated approaches solve the heat diffusion equation in the sediments [*Kuwagata et al*., 2008; *de la Fuente*, 2014a]; however, the numerical solution of the heat diffusion equation in the sediments increases the computational time which makes difficult to conduct long-term simulations. In this sense, the thermodynamic features of altiplanic wetlands, particularly water column depth of the order of 0–15 cm-deep, impose a constraint on the modeling that makes it difficult to use generalized models and parameterizations for these particular conditions.

In this article, we present a spectral model specifically designed for long-term simulations of the thermodynamics of shallow wetlands and in the limit case when the water depth goes to zero. This spectral model solves for the water and sediment temperature, as well as the heat, momentum, and mass exchanged with the atmosphere. The spectral model is so named because it decomposes the water temperature time series into a Fourier series [*Hussaini and Zang*, 1987], where the unknowns of the problem are the amplitudes of this decomposition. By casting this formulation in terms of periodic functions, the analytical solution of Stokes' second problem [*Batchelor*, 1967] is adopted to compute the sediment temperature. This formulation of the problem is also able to compute sediment temperature in the absence of the shallow water column, thus enabling the computation of potential evaporation rates from both the shallow wetland and the surrounding wetted area of the Salar. Although this spectral model is formulated for Andean Salars, it can be extended to similar shallow aquatic ecosystems that can be found in other regions on Earth [*Arias and Farfán*, 1997; *López-González et al*., 1997; *Timms*, 2005] and it can also be used to estimate the sediment temperature in shallow aquatic ecosystems that determines sediment diagenesis [*Cerco and Seitzinger*, 1997; *Jimenez et al*., 2008; *Paraska et al*., 2014]. Further theoretical aspects of the spectral model are discussed in *de la Fuente and Meruane* [2017].

This article is organized as follows. In section 2, we describe the governing equations and the spectral model, we list the iterative algorithm for computing the water and sediment temperature, and we detail the downscaling methodology required for the atmospheric reanalysis information. In section 3, we first discuss one of the parameters of the model, and then we present the results of the calibration of parameters of the model and the downscaling. Calibration was conducted by minimizing the root-mean-square error between the model results and MODIS land surface temperature [*Wan and Hulley*, 2015] between January

2000 and December 2016. Evaluation of the performance of the model in terms of the prediction of daily evaporation rates was made by the direct comparison between predicted daily evaporations and measured daily pan evaporation between 1964 and 2012. We show that changes in the wind pattern over the last decade have reduced the evaporation rates from the Salar by 10–20%. Finally, the manuscript ends with a discussion and a conclusion sections, where the advantages and limitations of the spectral model are discussed, and the main conclusions of this research are summarized.

2. Methods

2.1. Governing Equations

Let us consider a water column of height h with a vertically homogeneous water temperature T_w. Without considering horizontal advection or diffusion, the vertically integrated heat conservation equation is written as follows [*McCabe et al*., 2010; *McJannet et al*., 2013; *de la Fuente*, 2014a]:

$$\left(\rho c_p\right)_w h\frac{\partial T_w}{\partial t}=-H+H_g \tag{1}$$

where $\left(\rho c_p\right)_w$ is the heat capacity of the water ($\left(\rho c_p\right)_w \approx 4.4\times10^6$ J(m^3°K)$^{-1}$), and H (W m^{-2}) is the heat flux exchanged between the water and the atmosphere, which is written as [*Garratt*, 1992; *Bogan et al*., 2003]

$$H=-(1-\alpha)H_{sw}^{\downarrow}-H_{lw}^{\downarrow}+H_{lw}^{\uparrow}(T_w)+H_s(T_w)+H_l(T_w) \tag{2}$$

where α denotes the surface albedo of the wetland, $H_{sw}^{\downarrow}$ is the incident short-wave radiation from the sun, $H_{lw}^{\downarrow}$ is the incident long-wave radiation, $H_{lw}^{\uparrow}$ is the emitted long-wave radiation from the wetland, and $H_s(T_w)$ and $H_l(T_w)$ are the turbulent heat fluxes of sensible heat and latent heat, both depending on the water temperature. H is defined such that $H>0$ represents the case in which heat flows from the water to the atmosphere. Finally, H_g denotes the heat flux exchanges between water and sediments across the sediment-water interface (SWI) such that $H_g>0$ represents the case in which heat flows from the sediments to the water column. From the sediment-side of the SWI (at $z=0^-$), H_g can be evaluated as

$$H_g=-\kappa_s\left(\rho c_p\right)_s\left.\frac{\partial T_s}{\partial z}\right|_{z=0^-} \tag{3}$$

where κ_s is the thermal diffusion coefficient; $\left(\rho c_p\right)_s$ denotes the heat capacity of the sediments, valued between 1.4×10^6 and 3.8×10^6 J(m^3°K)$^{-1}$ [*Fang and Stefan*, 1998; *Prats et al*., 2011]; and T_s is the sediment temperature. The vertical axis z is defined such that the positive direction is upwards. From the water-side of the SWI (at $z=0^+$), H_g can be calculated as

$$H_g(t)=-k_t\left(\rho c_p\right)_w(T_w-T_{SWI}) \tag{4}$$

where T_{SWI} is the temperature at the SWI, and k_t is the heat transfer velocity depending on the bottom shear velocity and/or heat convection [*Necati*, 1977; *Martynenko and Khramtsov*, 2005; *Le and Papavassiliou*, 2006].

Here T_w, T_s, and T_{WSI} are obtained by solving equation (1) together with the heat diffusion equation in the sediments [e.g., *Smith*, 2002; *Prats et al*., 2011]:

$$\frac{\partial T_s}{\partial t}=\kappa_s\frac{\partial^2 T_s}{\partial z^2} \tag{5}$$

the heat flux continuity at the SWI, and the fact that the temperature at the SWI is continuous. That is, H_g calculated with equation (3) is equal to H_g calculated with equation (4), where $T_{WSI}=T_s(z=0^-)$. A zero temperature gradient is assumed at $z=-\infty$. One way to solve the set of two governing equations (equations (1) and (5)) is to discretize equation (5) with a finite volume scheme and solve the time dependence of the coupled system formed by equations (1) and (5) [*Kuwagata et al*., 2008; *de la Fuente*, 2014a]. The alternative solution proposed in this article is called a spectral model because it decomposes the water temperature into a Fourier series, in which the unknowns of the problem are the amplitudes of the frequency spectrum. As the problem is formulated in terms of a superposition of periodic solutions, the analytical solution

of Stokes' second problem [*Batchelor*, 1967] is adopted to compute the sediment temperature T_s; consequently, equation (3) can be directly evaluated. In this manner, the calculations for the water temperature computed with the spectral model consume a small fraction of the time spent using the standard approach of *de la Fuente* [2014a] (15 min a 3 days long simulation), and we ran a 57 year long-term thermodynamics simulation of Salar del Huasco with a computational time of less than 2 min on a standard desktop computer with an i5 quad-core processor and a Linux operating system.

2.2. Spectral Model

The spectral model considers that all the discrete variables can be expanded as a Fourier series of $2N+1$ terms, in which water temperature is written as

$$T_W(t) = \sum_{n=-N}^{N} T_{wn} e^{i\omega_n t} \tag{6}$$

where T_{wn} are the temperature amplitudes of the nth term of the Fourier expansion, $i=\sqrt{-1}$, $\omega_n = 2\pi n/(\Delta t(2N+1))$ is the frequency of the nth term of the Fourier expansion, and Δt is the time step of the temporal discretization of T_w. The temperature amplitudes of the expansions are constant and are the unknowns of the problem.

Then, since H is function of the water temperature itself, we propose an implicit treatment of H in the same way that source terms are treated in the finite volume method [*Patankar*, 1980; *Versteeg and Malalasekera*, 1995]. Consequently, H is linearized as

$$H = \alpha_H + \beta_H T_w \tag{7}$$

where α_H is a time series, and β_H should be a constant value. Accordingly to *Patankar* [1980], the linearization of the source terms required to acknowledge the implicit dependence of H on T_w, while retaining the advantages of solving the discretized equation based on numerical techniques developed for linear algebraic equations (Fourier decomposition in the context of the spectral model). With this linearization of the source term, α_H is expanded into a Fourier series as follows:

$$\alpha_H = \sum_{n=-N}^{N} H_n e^{i\omega_n t} \tag{8}$$

where the coefficients H_n can be obtained using a fast Fourier transform (*fft*) of α_H. In particular, if $Y = fft(\alpha_H)$, the nth amplitude H_n is computed as $H_n = Y_n/(2N+1)$. The linearization of H enables feedback between the water temperature and H to be included, which provides a solution for the frequency-independent term $(n=0)$ of the Fourier decomposition. This aspect will be discussed again once the final solution is obtained.

In the sediments, the temperature at the SWI is also expanded in a Fourier series as

$$T_{SWI} = \sum_{n=-N}^{N} T_{sn} e^{i\omega_n t} \tag{9}$$

where T_{sn} are the SWI temperature amplitudes of the nth term of the Fourier expansion. The temperature at the SWI is the boundary condition for the heat diffusion linear equation in the sediments (equation (5)). As a consequence, the sediment temperature can also be expanded in a series of solutions such that each one of them is the solution of the well-known Stokes' second problem, which describes the solution of the diffusion equation forced by a periodic Dirichlet function in a semi-infinite domain [*Batchelor*, 1967; *Prats et al.*, 2011]. Considering this, the sediment temperature can be written as

$$T_s(z,t) = \sum_{n=-N}^{N} T_{sn} e^{i\omega_n t} e^{(1+s_n i)\alpha_n z} \tag{10}$$

where $\alpha_n = \sqrt{abs(\omega_n)/2\kappa_s}$, and s_n is the sign of n. Note that the SWI is defined at $z=0$, and sediments are located at negative values of z. Then, equation (3) can be directly evaluated to obtain

$$H_g = -\kappa_s (\rho c_p)_s \sum_{n=-N}^{N} \alpha_n T_{sn} e^{i\omega_n t} (1+s_n i) \tag{11}$$

for the sediment side of the SWI, while for the water-side of the SWI, equation (4) can be written as

$$H_g = -k_t\left(\rho c_p\right)_w \sum_{n=-N}^{N} (T_{wn} - T_{sn}) e^{i\omega_n t} \tag{12}$$

In this manner, all the terms of the coupled system formed by equations (1) and (5) are written as Fourier expansions, and by replacing equation (9) in equation (1), the latter is written as

$$\sum_{n=-N}^{N} i\Omega_n T_{wn} e^{i\omega_n t} = \sum_{n=-N}^{N} \left(-H_n - \beta_H T_{wn} - \kappa_s \left(\rho c_p\right)_s \alpha_n T_{sn}(1+s_n i)\right) e^{i\omega_n t} \tag{13}$$

where $\Omega_n = \omega_n h\left(\rho c_p\right)_w$. Furthermore, flux continuity at the SWI provides a second equation written as

$$-\kappa_s \left(\rho c_p\right)_s \sum_{n=-N}^{N} \alpha_n T_{sn} e^{i\omega_n t}(1+s_n i) = k_t\left(\rho c_p\right)_w \sum_{n=-N}^{N} (T_{wn} - T_{sn}) e^{i\omega_n t} \tag{14}$$

Given this, the complex amplitudes are written as

$$T_{wn} = -H_n \left(i\Omega_n + K\left(1 - \frac{K}{K + (1+is_n)D_n}\right) + \beta_H \right)^{-1} \tag{15}$$

and

$$T_{sn} = \frac{K}{K + (1+is_n)D_n} T_{wn} \tag{16}$$

where $K = k_t\left(\rho c_p\right)_w$ and $D_n = \left(\rho c_p\right)_s k_s \alpha_n$.

Equation (13) shows the advantage of the linearization of H in the context of reaching a solution for the frequency-independent term ($n=0$). In particular, if $\omega_n = 0$, both Ω_n and α_n are equal to 0, and the solution for $T_{w0} = -H_0/\beta_H$ is available. On the contrary, if an explicit formulation is used to represent H in terms of T_w, the solution for T_{w0} would not exist. Another aspect that must be noticed is the fact that, for shallow flows, an important fraction of the downward solar radiation is absorbed in the sediments [*de la Fuente*, 2014a], while we assume that all of the effective solar radiation ($(1-\alpha)H_{sw}^{\downarrow}$) is retained in the water column without including heat absorption in the sediments. However, *de la Fuente* [2014a] also showed that retaining all of the heat in the water produces a small difference in the simulated water temperature, with a standard deviation of 0.75°C between the water temperature with and without considering heat absorption in the sediments, which is a small value in the context of a diurnal thermal oscillation of 25°C. Consequently, it is acceptable to make this assumption as it enables using the solution of the second problem of Stokes for the heat diffusion in the sediments, which makes the spectral model very efficient in terms of computational time and resources. Further details on the spectral model and the dimensionless numbers that characterize the dynamics are found in *de la Fuente and Meruane* [2017].

Finally, an interesting scenario is related to $h=0$, which represents the case in which the soil temperature is computed in the absence of a shallow water column. This case is reduced to flux continuity at the sediment surface ($z = 0$), written as

$$-H + H_g = 0 \tag{17}$$

and the complex amplitudes for the temperature at $z=0$ are given by $T_{sn} = T_{wn}$ and

$$T_{wn} = \frac{-H_n}{\beta_H + D_n(1+s_n i)} \tag{18}$$

2.3. Iterative Algorithm

An iterative algorithm is required to deal with the nonlinear nature of the heat flux exchanged with the atmosphere. This iterative algorithm for the spectral model considers H to be a nonlinear function of T_w that is computed with Kansas's experimental parametrizations of the Monin-Obukhov similarity functions for H_s and H_l, the Charnock roughness length [*Garratt*, 1992; *Imberger*, 2013], and the other parametrization used by *Bogan et al.* [2003] and *de la Fuente* [2014a] for incident and emitted long-wave radiation. The linearization of H into the form of equation (7) represents the heat flux exchanged with the atmosphere for the iteration k + 1 as

$$H^{(k+1)} = H^* + \beta_H \left(T_w^{(k+1)} - T_w^{(k)}\right) \tag{19}$$

where $H^* = H\left(T_w^{(k)}\right)$ is H evaluated with the water temperature of iteration k. As a consequence, it is shown that β_H is a representative value of $\partial H/\partial T_w$, which, for simplicity, can be estimated as

$$\frac{\partial H}{\partial T_w} \approx \frac{\left(H\left(T_w^{(k)} + \epsilon\right) - H\left(T_w^{(k)}\right)\right)}{\epsilon} \tag{20}$$

where ϵ is a small value of the order 10^{-5}°C. In the result section, further discussion on the value of β_H is provided; however, it is important to notice here that equation (19) shows that, if the convergence of the model is good, ($T_w^{(k+1)} \approx T_w^{(k)}$), $H^{(k+1)}$ is equal to $H^* = H\left(T_w^{(k)}\right)$, which computes all the nonlinear dependency of H as a function of T_w. Therefore, $T_w^{(k+1)} \approx T_w^{(k)}$, and the value of the coefficient β_H should not be relevant in the presentation of H and thus the solution for T_w. Finally, the time series α_H of equation (7), which is updated for each iteration, is written as

$$\alpha_H^{(k)} = H^* - \beta_H T_w^{(k)} \tag{21}$$

Furthermore, a constant characteristic value of k_t (hereinafter called k_t^*) is required in the spectral model for $h > 0$ (equations (15) and (16)). However, this transfer velocity actually varies within the day and may also be driven by convection [*Necati*, 1977; *de la Fuente*, 2014a; *de la Fuente et al*., 2016], such as k_t^* should represents the actual conditions of the shallow wetland. For choosing the representative value k_t^*, we first compute the time series of k_t and use it to define k_t^*. Here we adopted the standard parameterizations of heat conduction during free convection that can be found in *Necati* [1977], which computed k_t as

$$\frac{k_t h}{\kappa} = \alpha_{Ra} R_a^{\beta_{Ra}} \tag{22}$$

where $R_a = g\beta h^3 \Delta T/(Pr\ \kappa^2)$ denotes the Rayleight number, where g is the gravity acceleration, β the thermal expansion coefficient of water, $\Delta T = T_{WSI}^{(k)} - T_W^{(k)}$, Pr is the Prandtl number and κ is the molecular thermal diffusivity coefficient of water. In equation (22), α_{Ra} and β_{Ra} are empirical constant whose value depends on the conditions of the problem (Table 1). On the other hand, when turbulent heat exchanges across the water-sediment interface is dominated by shear friction induced by the wind, k_t was computed as

$$k_t = \frac{1}{\alpha_{kt}}\ u_* Pr^{-\beta_{kt}} \tag{23}$$

where u_* denotes the bottom shear velocity that was considered equal to the wind shear velocity as a Couette flow was assumed, and α_{kt} and β_{kt} are empirical constants whose values are listed in Table 1. In practical terms, the maximum value between equations (22) and (23) was used for k_t at one particular time. Consequently, the value of k_t^* is also updated in any iteration, and two different values were used to estimate it: the average k_t ($k_t^* = avg(k_t)$) and

$$\frac{1}{k_t^*} = \mathrm{avg}\left(\frac{1}{k_t}\right) \tag{24}$$

which enhances the influence of small values of k_t in the characteristic transfer velocity. The influence of this assumption is discussed in the results section. This step is not required for the case of $h = 0$. The function $\mathrm{avg}(\cdot)$ denotes the average function of the argument.

Table 1. Characterized Values of Parameters of Equations (22) and (23)[a]

Equation	Parameter	Values	
Equation (22)	$(\alpha_{Ra}, \beta_{Ra})$	(0.14, 1/3): horizontal plate $R_a > 2\times10^7$ (*)	*Necati* [1977]
		(0.54,1/4): horizontal plate, $10^5 > R_a > 2\times10^7$ (*)	*Necati* [1977]
Equation (23)	$(\alpha_{u_*}, \beta_{u_*})$	(13.6, 0.612) (*)	*Le and Papavassiliou* [2006]
		(6–50, 2/3)	*Dade* [1993], *Hondzo et al*. [2005], *O'Connor and Hondzo* [2008], and *de la Fuente et al*. [2016]

[a]Cells with (*) indicate parametrization that is used in this research.

Finally, the iteration starts with a constant and arbitrary water temperature $T_w^{(0)}=10°C$ that is used to compute the first time series of $\alpha_H^{(0)}$ that forces the model. The results presented in this article are not sensible on this starting point, and this was verified by conducting simulations with starting temperature of 5, 10, and 20°C (not shown here). It is important to notice that the starting point should not be understood as the initial condition of the simulation. This is because the spectral model do not requires an initial condition as it computes the periodic thermal oscillations of the water temperature instead of the time series of water temperature. Phase and amplitude of the thermal oscillations are determined by the balance among heat exchanges with the atmosphere and the sediments, and the thermal inertial of the water column itself [*de la Fuente and Meruane*, 2017]. Given these assumptions, for the iteration $k+1$, the iterative algorithm for the spectral model is described as follows:

1. Compute H as a function of $T_w^{(k)}$ and then compute $\alpha_H^{(k)}$ with equation (21).
2. Compute H_n using a Fourier transform of $\alpha_H^{(k)}$. In particular, if $Y=fft(H)$, then $H_n=Y_n/(2N+1)$.
3. Compute T_{wn} and T_{sn} using equations (15) and (16). Equation (18) should be used in the case of solving soil temperature in the absence of the shallow water column ($h=0$).
4. Compute the water temperature for the iteration $k+1$, $T_w^{(k+1)}$ in equation (6). This can be performed with the inverse Fourier transform (*ifft*) of T_{wn}. In particular, $T_w=ifft(T_{wn})\ (2N+1)$. However, to increase the convergence of the solution, the use of an underrelaxation factor, r, is recommended, such that $T_w^{(k+1)}$ is finally computed as
$$T_w^{(k+1)}=(1-r)\ ifft(T_{wn})(2N+1)+r\ T_w^{(k)} \tag{25}$$
$r=0.7$ was used in this article.
5. Update k_t^*.
6. Check the convergence of the solution and return to step 1 if required. The convergence of the model was quantified by looking at the standard deviation between $T_w^{(k+1)}$ and $T_w^{(k)}$, and a threshold value of 10^{-2}°C can be used to stop the simulation.

2.4. Field Observations and Meteorological Downscaling

The analysis is focused on Salar del Huasco (Figure 1), located 3800 m above sea level (20.274°S, 68.883°W), where several research studies have been conducted [*Herrera et al*., 2009; *Dorador et al*., 2010; *de la Fuente*, 2014a; *Hernández-López et al*., 2016]. For the purposes of this article, a combination of field observations, satellite products and atmospheric reanalysis are used to calibrate the downscaling and the parameters of the model, and also to evaluate the performance of the spectral model (Figure 2).

The spectral model requires time series of meteorological variables of air temperature and humidity, wind speed and direction, and incident solar radiation. One standard meteorological station was installed in September 2015 in Salar del Huasco (white circle, Figure 1a), where meteorological variables are measured every 1 h. To extend the length of the meteorological time series that forces the spectral model, we used NCEP-NCAR atmospheric reanalysis [*Kalnay et al*., 1996]. This information is available every 6 h for a regular mesh of 192×94 elements (spaced ∼200 km apart at this latitude). We used the air temperature and mixing ratio of water vapor at 2 m above the land surface, wind speed at 10 m above the land surface, percentage of cloud cover, and atmospheric pressure at the land surface. All of this information was interpolated to the latitude-longitude coordinate of Salar del Huasco using the inverse square distance method. Then, a linear regression was established between measurements at the meteorological station and the atmospheric reanalysis. The performance of this downscaling for representing field observations is shown in Figure 3a for wind speed, Figure 3b for mixing ratio, and Figure 3c for air temperature. Figure 3c also shows, in gray circles, a comparison between the daily average air temperature measured between August 1981 and July 1982 at the location identified with an open white circle in Figure 1a. The solid black line indicates the linear fit, while the dashed line represents the 95% confident interval of the estimation. Finally, to properly account for the incident solar radiation, the 6 h information from the NCEP-NCAR reanalysis was linearly interpolated every hour, and the downward short-wave solar radiation was estimated following *Stull* [1988, chapter 7]. Statistics of the downscaling are given in Table 2.

2.5. Numerical Setup

The calibration of the parameters of the spectral model was performed based on the direct comparison between the predicted water temperature and the land surface temperature (LST) product of the MODIS

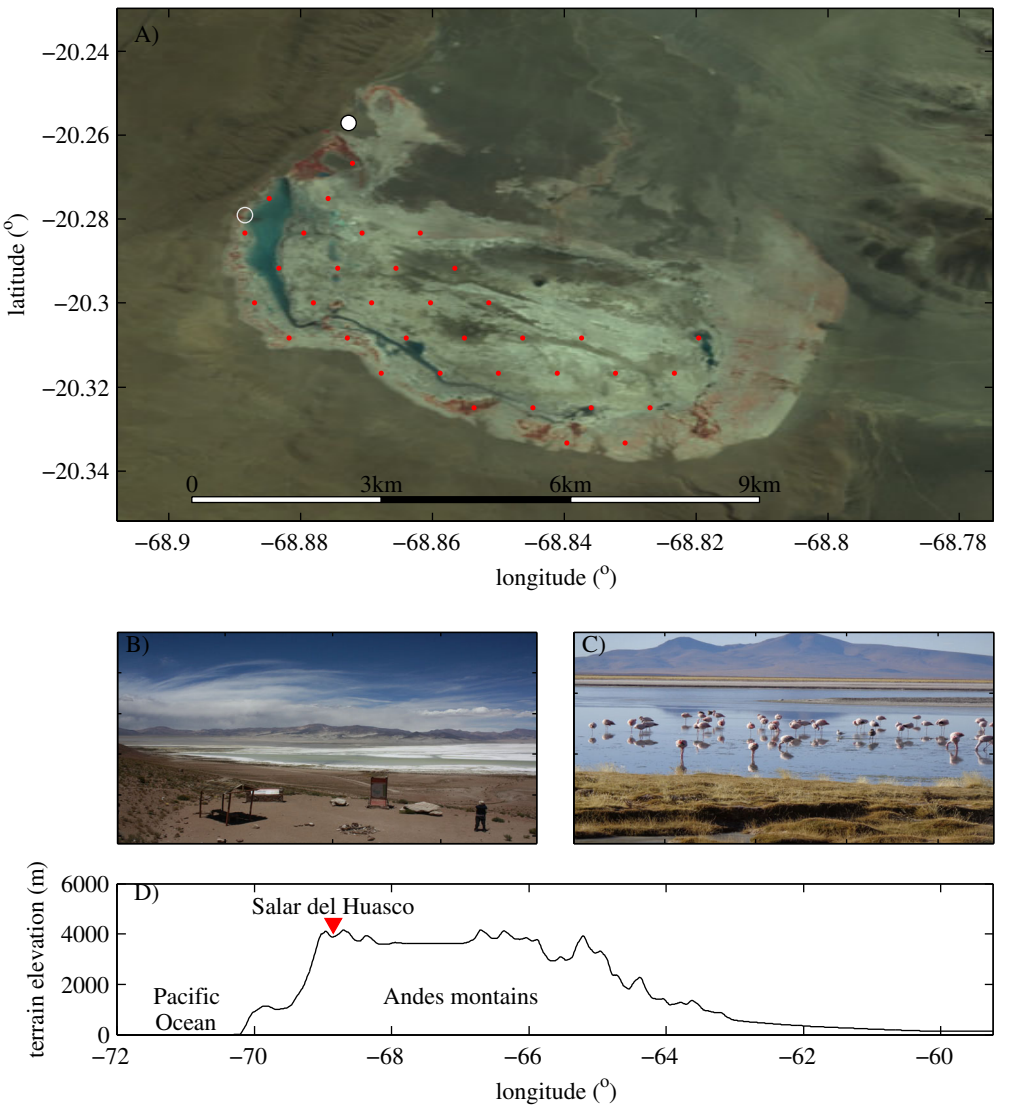

Figure 1. (a) Satellite image of Salar del Huasco and the locations of the meteorological stations installed in October 2012 (filled white circles) and 1981–1982 (open white circles). Red dots indicate the location of the land surface temperature of a MODIS satellite. (b, c) Pictures of the study site. (d) Location of Salar del Huasco in the context of a topographic profile along the latitude 20.3°S.

satellite. MODIS satellite estimates LST in a grid with a spatial resolution of 1 km, providing two observations in the day, characterizing daytime (at approximately 10 am local solar time) and night time (at approximately 22 h local solar time). Version 006 of the satellite product was used [*Wan and Hulley*, 2015], and the space average of observations at grid points indicated as red dots in Figure 1a was used as the representative LST of Salar del Huasco. The simulated temperature every hour was linearly interpolated to the corresponding time of the MODIS observation, and the objective of the calibration was to minimize the root-mean-square error between MODIS observations and the simulated temperature T_w by the spectral model. The calibration period is between January 2000 and December 2016, and in total, we calibrated four physical parameters of the spectral model: (i) the sediment heat capacity $(\rho c_p)_s$, which takes values between 1.4 $\times$ 10^6 and 3.8 $\times$ 10^6 J(m^3°K)$^{-1}$ [*Fang and Stefan*, 1998; *Prats et al*., 2011]; (ii) the thermal diffusion coefficient in the sediments, k_s, between 0.01 and 0.11 m^2 d^{-1} [*Fang and Stefan*, 1998; *Prats et al*., 2011]; (iii) the surface albedo, which can take values between 0.03 for clear and deep waters [*Bogan et al*., 2003] and 0.17 for shallow saline lakes [*de la Fuente*, 2014a]; and (iv) the representative water depth, h, whose value ranges between 0 and 15 cm. The water heat capacity was assumed to be constant and equal to 4.4 $\times$ 10^6 J(m^3°K)$^{-1}$. In section 3, it is shown that the model result is independent of β_H and k_t^*. Finally, the uncertainty

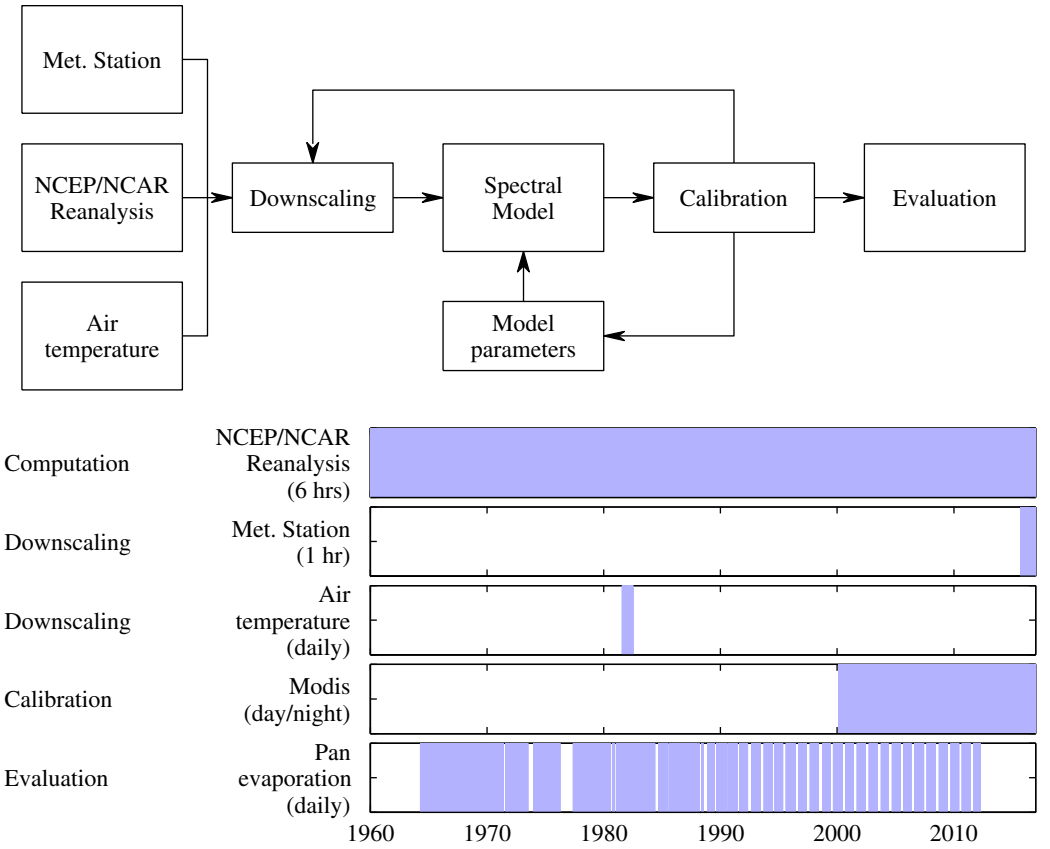

Figure 2. Layout for the calibration methodology and available information.

in the atmospheric downscaling (Figure 3) was included by fitting three dimensionless parameters of the downscaling (δ_u, δ_q, and δ_{T_a}) that take values between −1 and 1 and varying the estimation of the downscaled variables (U_{10}, q, and T_a) within the 95% confidence interval delimited by the dashed lines of

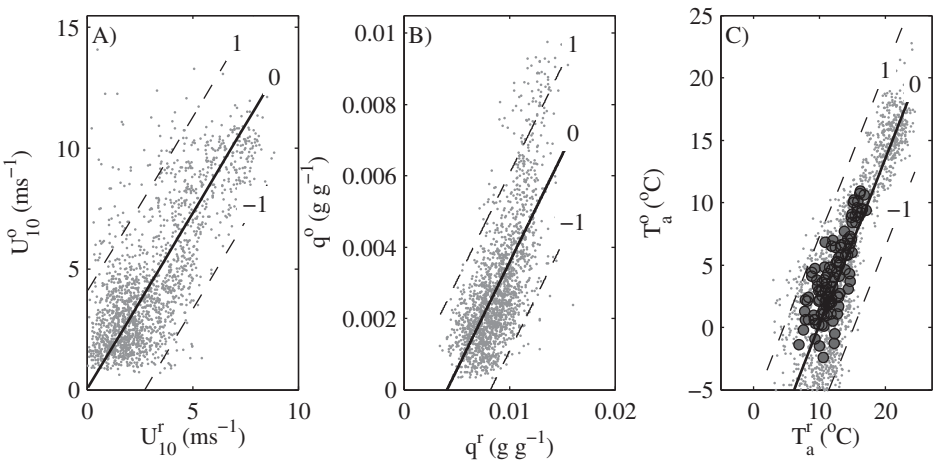

Figure 3. (a) Comparison between the interpolated wind speed at 10 m from the reanalysis (with superscript *r*) and observations (with superscript *o*) made at the meteorological stations. Solid lines plot the linear fit that minimizes the root-mean-squared error, while dashed lines define the 95% confidence interval of the estimation. The numbers −1, 0, and 1 denote the value of the dimensionless parameter that is calibrated to account for uncertainty in the downscaling process. (b) Similar to Figure 3a, for the mixing ratio. (c) Similar to Figure 3a, for the air temperature. Gray circles plot measurements for September 2015 to December 2016, and darker circles indicate measurements made in 1982–1983.

Table 2. Statistics of Meteorological Downscaling

	Nash-Sutcliffe Coefficient (NSE)	Willmott Index of Agreement	Correlation Coefficient	Average Bias (Observed-Downscaling)
U_{10}	0.50	0.75	0.87	−0.06
q	0.49	0.70	0.75	0.00
T_a	0.76	0.87	0.92	0.00

Figure 3. The numbers in Figure 3 are the values of these dimensionless numbers in the range between −1 and 1. The index of agreement, S [*Willmott*, 1981], of the linear regression is given in Table 2.

Evaluation of the spectral model was performed based on diurnal pan evaporation, a record that is available between 1964 and 2012 for Collacagua, which is a small village located in the Salar del Huasco catchment at 3800 m above sea level and 20 km north of Salar del Huasco. The actual evaporation rates used in this article were computed with a pan coefficient equal to 0.65 [*Risacher et al*., 2003]. It is reminded that the evaporation, E_v, was computed with Kansas's experimental parametrizations of the Monin-Obukhov similarity functions and the Charnock roughness length [*Garratt*, 1992; *Imberger*, 2013]. The latent heat flux of evaporation of equation (2) was computed as $H_l=\rho L_v E_v$, where L_v is the latent heat of evaporation, and ρ is the water density.

The sensitivity analysis of the results with respect to the calibrated parameters is conducted based on the dimensionless sensitivity, σ_{i,x_j}, defined as [*Jørgensen and Bendoricchio*, 2001]

$$\sigma_{i,x_j}=100\frac{x_j^*}{\sigma_i^*}\frac{\partial\sigma_i}{\partial x_j}\Bigg|_{x_j^*} \tag{26}$$

where σ_i denotes the parameter that is studied, x_j denotes the jth coefficient that was calibrated (h, $(\rho c_p)_s$, albedo, k_s, δ_u, δ_q, and δ_{T_a}), and x_j^* and σ_i^* denote the corresponding variables evaluated at the calibrated value of x_j. σ_{i,x_j} is expressed as a percentage, and it is understood as the percentage of change in σ_i given a 100% change in the calibrated parameter x_j. Here we studied the influence of the calibrated coefficients on the root-mean-squared error of the LST (σ_{rms}), the average annual evaporation during the evaporation period (σ_{Ev}), the annual temperature ($\sigma_{\bar{T}_w}$), and the average diurnal thermal oscillation ($\sigma_{\Delta T_w}$).

3. Results

3.1. Linearization Coefficient β_H

The linearization coefficient must be defined before the simulations. This coefficient is a representative value of $\partial H/\partial T_w$ and should be constant. Figure 4a shows the frequency distribution of $\partial H/\partial T_w$ computed with the spectral model with β_H between 5 and 90 W(m^2°C)$^{-1}$ [*de la Fuente and Meruane*, 2017], h=5 cm, $(\rho c_p)_s$= 2.2 ×10^6 J(m^3°K)$^{-1}$, albedo = 0.17, k_s=0.035 m^2 d^{-1} [see *de la Fuente*, 2014a, 2014b] and $\delta_u=\delta_q=\delta_{T_a}=0$. Figure 4a shows that $\partial H/\partial T_w$ takes values between 5.1 and 68.9 W(m^2°C)$^{-1}$ (99% of the points), with a median value of 17 W/m^2/°C. Considering this result, a standard reference value of β_H=20 W(m^2°C)$^{-1}$ was chosen. Then, to quantify the influence of β_H in T_w, Figure 4b shows the 1% and 50% exceedance of the absolute difference between the computed T_w with β_H=20 W(m^2°C)$^{-1}$ and other values of β_H between 5 and 90 W(m^2°C)$^{-1}$. The absolute difference between the water temperature computed for different values of the parameter β_H shows a small deviation (<0.01°C) with respect to the water temperature estimated for β_H=20 W(m^2°C)$^{-1}$, which proves that the results of the spectral model are independent of the value of β_H. Following this conclusion, β_H=20 W(m^2°C)$^{-1}$ is hereinafter used for all the simulations.

3.2. Calibration and Sensitivity Analysis

The calibration was performed by looking at the best representation of MODIS LST measurements with the spectral model, in terms of the minimization of the root-mean-square error. Figure 5a presents a direct comparison of the time series of the observed LST and simulated T_w for the fitted parameters detailed in Table 3, and k_t^*=avg(k_t)=8.7 m d^{-1}. The 95% confidence interval of the fitted coefficient was computed following [*Seber and Wild*, 2003; *de la Fuente*, 2014b]. The index of agreement [*Willmott*, 1981] of the estimation of the land surface temperature is equal to 0.96, the correlation coefficient is 0.94, the Nash-Sutcliffe

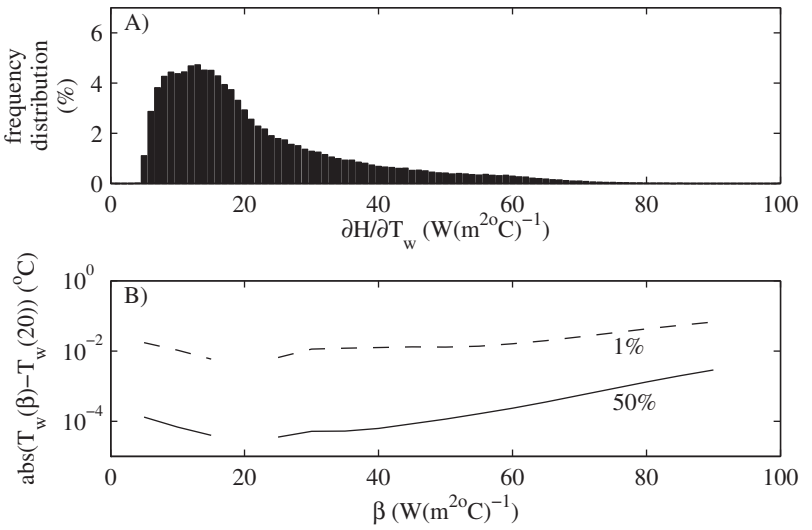

Figure 4. (a) Histogram of values of $\partial H/\partial T_w$. (b) Difference between the predicted water temperatures for different values of β_H, with respect to the water temperature estimated for $\beta_H = 20$ W(m^{2o}K)$^{-1}$. Dashed and solid lines were computed for different exceedance probabilities indicated in the plot.

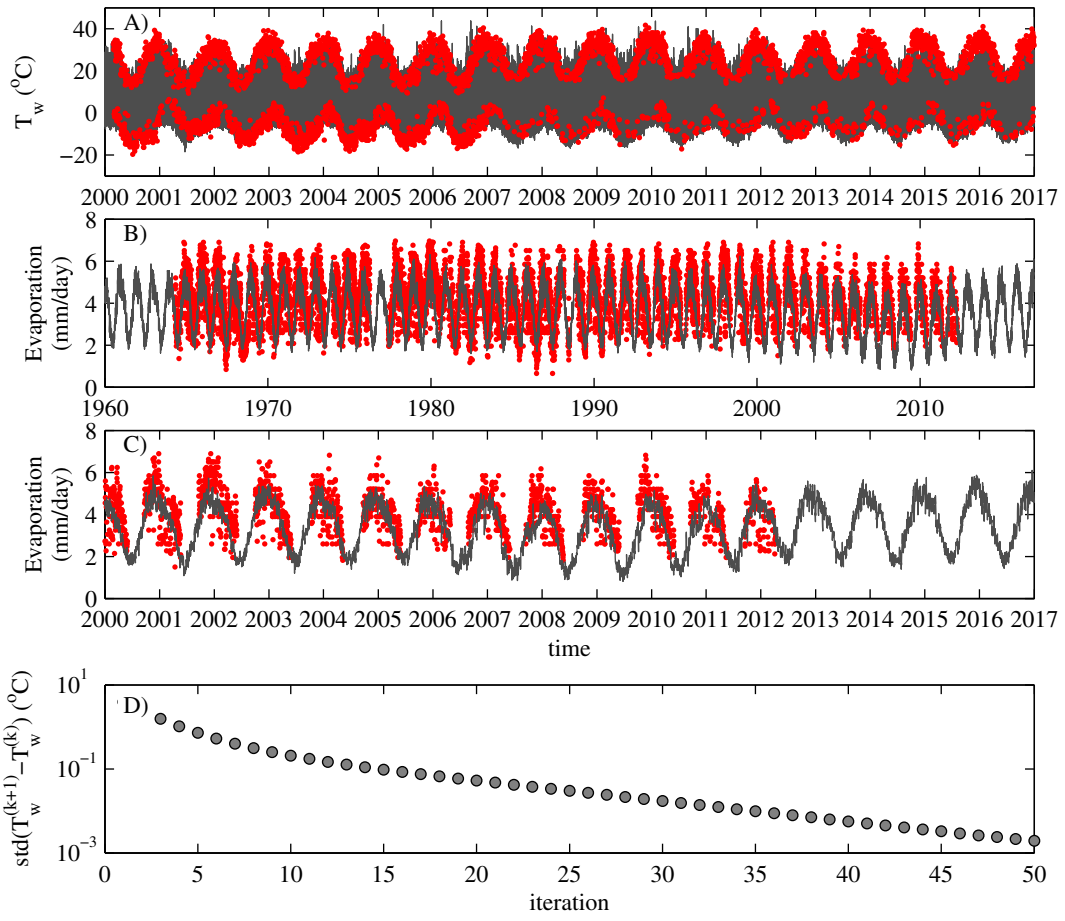

Figure 5. (a) Time series of observed (red dots) and simulated (black line) land surface temperatures of Salar del Huasco for fitted parameters of Table 1. (b) Time series of observed (red dots) and simulated (black line) daily evaporations for the entire period of simulation (1960–2016). (c) Similar to Figure 5b for the calibration period between 2000 and 2016. (d) Evolution of the convergence of the spectral model as a function of the number of iterations for the 67 yearlong simulation.

Table 3. Calibrated Values of the Seven x_j Parameters (h, $(\rho c_p)_s$, Albedo, k_s, δ_u, δ_q, and δ_{T_a}) Depending on the Definition of k_t^* as avg(k_t) or Equation (21)

		Units	x_j^* k_t^*=avg(k_t)	x_j^* k_t^* of Equation (21)
Parameters of the spectral model	h	mm	4 ± 3	$<1 \pm 2$
	$(\rho c_p)_s$	$\times 10^6$ J (m^{3}K)$^{-1}$	2.12 ± 0.13	2.16 ± 0.09
	Albedo		0.13 ± 0.01	0.13 ± 0.02
	k_s	m^2 d^{-1}	0.011 ± 0.00	0.013 ± 0.001
Downscaling	δ_q		0.48 ± 0.16	0.43 ± 0.16
	δ_{T_a}		-0.44 ± 0.07	-0.44 ± 0.07
	δ_u		0.06 ± 0.03	0.05 ± 0.01

model efficiency coefficient (NSE) is 0.88, and the average bias is −0.64°C (average observations larger than average simulations). Moreover, a direct comparison between the predicted and simulated daily evaporation is shown in Figures 5b and 5c for the entire record between 1964 and 2012 and for the calibration period, respectively. The index of agreement for the daily evaporation during the entire period between 1964 and 2012 is 0.80, the correlation coefficient is 0.66, the NSE coefficient is 0.30, and the average bias is −0.35 mm d^{-1} (the model predicts smaller evaporations than the measurements). Finally, the results shown in Figure 5 were obtained considering 50 iterations, and the convergence of the solution is shown in Figure 5d. The standard deviation between $T_w^{(k+1)}$ and $T_w^{(k)}$ was 0.0019°C, while the maximum difference between $T_w^{(k+1)}$ and $T_w^{(k)}$ was 0.17°C, which represent the standard and maximum error in the representation of H as 0.04 and 3.4 W m^{-2}, respectively. The good agreement between the observed and simulated temperatures shown in Figure 5a supports the use of the spectral model for computing land surface temperature in altiplanic wetlands. However, the NSE coefficient of the daily evaporations is small and equal to 0.3. This coefficient quantifies the standard error in the estimation normalized with the standard deviation of the observations. Based on the visual comparison between observed and predicted evaporations (Figures 5b and 5c), this small value of the NSE coefficient indicates that the model is not fully capturing the natural variation in this parameter. This lack of representation of natural variability in daily evaporation can be attributed to the downscaling process that did not fully capture the day-to-day variation in atmospheric forcing (Figure 3); the assumption of using a constant albedo and/or other aspects that are not necessarily related to the spectral model itself. Despite of this limitation in the representation of the day-to-day variation in the daily evaporation, in the following "long-term perspective" section we show that the spectral model is able to represents the observed seasonal and climatic trend in the potential evaporation.

With respect to the calibration process, Table 3 shows the values of the 7 calibrated parameters for the two different alternatives adopted to compute k_t^*. The use of $k_t^*=avg(k_t)$ provided a characteristic heat transfer velocity k_t^*=8.7 m d^{-1}, while k_t^* with equation (24) yields k_t^*=0.5 m d^{-1} (1 order of magnitude smaller than k_t^*=avg(k_t)). However, the obtained results showed no difference depending on which definition of k_t^* is used. This response is related to the fact that heat transport across the water-sediment interface is more controlled by heat diffusion in the sediments than by turbulent transport in the water column [*de la Fuente and Meruane*, 2017]. In particular, as the representative water depth is very small, the dimensionless number $k_t^*(\Omega h)^{-1}$ is very large [*de la Fuente and Meruane*, 2017]; consequently, the spectral model is not very sensitive to k_t^*.

Table 4 shows the values of the dimensionless sensitivity defined in equation (26), and allows for quantifying the influence of the parameters on the response of the spectral model to be quantified. Cells marked in

Table 4. Result of the Sensitivity Analysis[a]

		σ_{Ev,x_j} (%)	σ_{rms,x_j} (%)	$\sigma_{\bar{T}_w,x_j}$ (%)	$\sigma_{\Delta T_w,x_j}$ (%)
Parameters of the spectral model	h	0.3	0.9	0.7	*1.4*
	$(\rho c_p)_s$	*–8.7*	*3.8*	**33.0**	**–24.8**
	Albedo	**–20.9**	*2.0*	**–27.4**	*–8.4*
	k_s	*–4.3*	*1.9*	**16.5**	**–12.4**
Downscaling	δ_q	*–6.1*	*1.4*	**14.6**	−0.5
	δ_{T_a}	*9.7*	*2.1*	**32.1**	**–1.3**
	δ_u	0.9	0.1	*–6.3*	*–2.1*

[a]Bold cells highlight high sensitivity with values of $|\sigma_{i,x_j}| > 10$, while entries in italic highlight moderate sensitivity with $10 > |\sigma_{i,x_j}| > 1$. σ_{i,x_j} is defined in equation (26) and was computed with k_t^*=avg(k_t).

blue in Table 3 are identified as the most sensible parameters with the corresponding sensibility index larger than 10%, which means that an increase of 100% of the calibrated parameter would produce changes in the objective variable (evaporation, air temperature, and diurnal thermal oscillation) of more than 10%. With respect to the downscaling parameters, as expected, an increase in wind speed (δ_u) produces an increase in the evaporation ($\sigma_{Ev,x_j}>0$) and a cooling of the average water temperature ($\sigma_{\bar{T}_w,x_j}<0$); and an increase in the air humidity (δ_q) reduces the evaporation, thus reducing heat losses by latent heat and increasing the average water temperature. With respect to the parameters of the spectral model itself, the estimation of water temperature and potential evaporation are most sensitive to the heat capacity of the sediments and the albedo. On the one hand, an increase in $(\rho c_p)_s$ produces an increase in the average temperature and a reduction in the diurnal thermal amplitude. A similar response is observed in k_s, which can be explained by the fact that heat diffusion is the sediments is proportional to $k_s(\rho c_p)_s$ (see equation (16) and the definition of D_n). On the other hand, the computed potential evaporation is sensible to the albedo such that an increase in this parameter reduces the amount of heat that is retained in the water column and the sediments, thus reducing the evaporation, the average water temperature and the thermal amplitude. Finally, the calibrated water depth was nearly equal to 0, and the evaluated objective variables are not sensitive to this parameter.

3.3. Long-Term Perspective

Figure 6a shows the time series of the annual average land surface temperature simulated by the spectral model. This figure shows that the parameter has monotonically increased with time at a rate of 0.25°C per decade (dashed line in Figure 6a). This trend can be attributed to global warming and evidences the fact

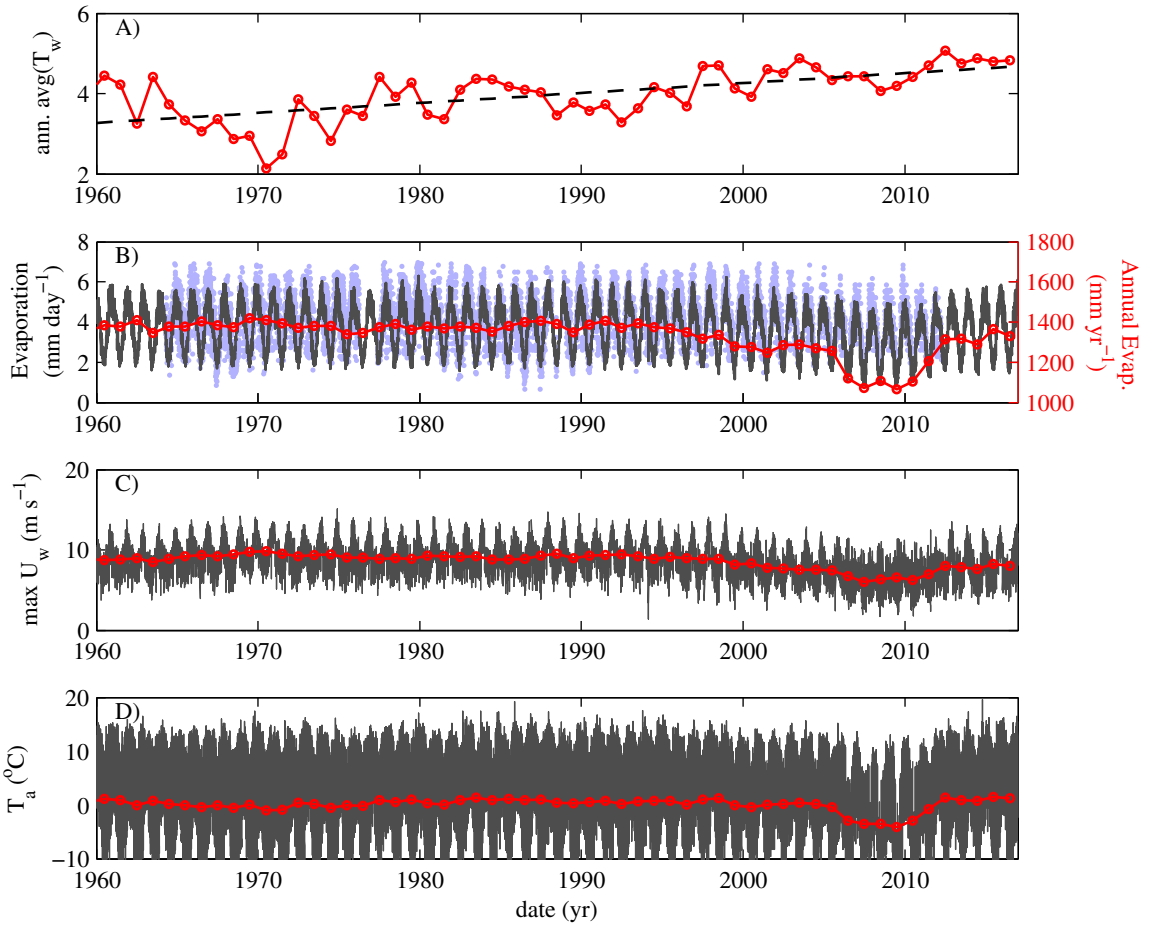

Figure 6. Simulation results. (a) Time series of the annual average land surface temperature of Salar del Huasco (red line). The dashed line indicates trends with a slope of 0.25°C per decade. (b) Time series of the simulated (black line) and measured daily evaporations (light blue dots) and annual average potential evaporations (red line). (c, d) Times series of the maximum daily wind speed and air temperature (black lines) and annual average (red line), from the atmospheric reanalysis after downscaling.

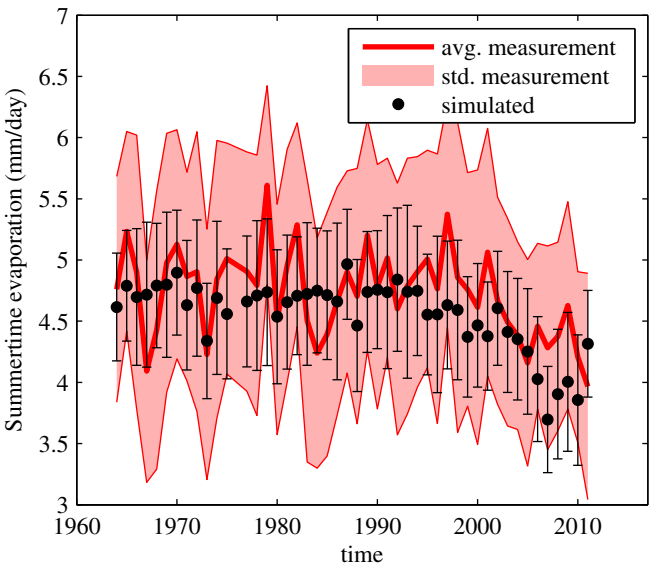

Figure 7. Comparison between the observed (red line) and simulated (black circles) averaged daily evaporations between September and March. The light red area denotes the standard deviation of the measurements, while the error bars represent the standard deviation of the simulated daily evaporation.

that the spectral model can represent this type of trend despite the formulation based on periodic functions. This is based on the fact that the Fourier transform is based on an orthogonal base of functions, such that any discrete function can be decomposed into a Fourier series without being required to be periodic [e.g., *Mertins*, 1999]. Furthermore, Figure 6b shows the time series of the simulated (black line) and observed (light blue bars) daily evaporation, and the total annual evaporation is shown via a thick red line. It is observed that, in the last few decades, the total annual evaporation has decreased by 10–20% with respect to the values simulated for the last decades of the twentieth century (≈1400 mm yr^{-1}). These changes can be attributed to changes in wind speed (Figure 6c) and air temperature (Figure 6d). This reduction in the annual evaporation is congruent with observations of daily evaporation measured in Collacagua, which is better observed in Figure 7 that plots the average evaporation during austral summer (September–March) for simulated (red thick line) and measured (black circles) data, in which the red area denotes the standard deviation of the observations and the black error bars the standard deviation of the simulated evaporation. It is important to note that between 1995 and 2012, measurements of the daily evaporation were conducted only between September and March.

To see the consistency of this result in the regional context, Figure 8 frames the percentage of changes between the decadal averages of the evaporation with respect to the average evaporation between 1960 and 1969. These results were computed with the NCEP-NCAR reanalysis information, and the calibrated parameters of the spectral model. It is observed that temporal changes in the evaporation have been intensified over time in the study area, with a persistent reduction in the potential evaporation in the second half

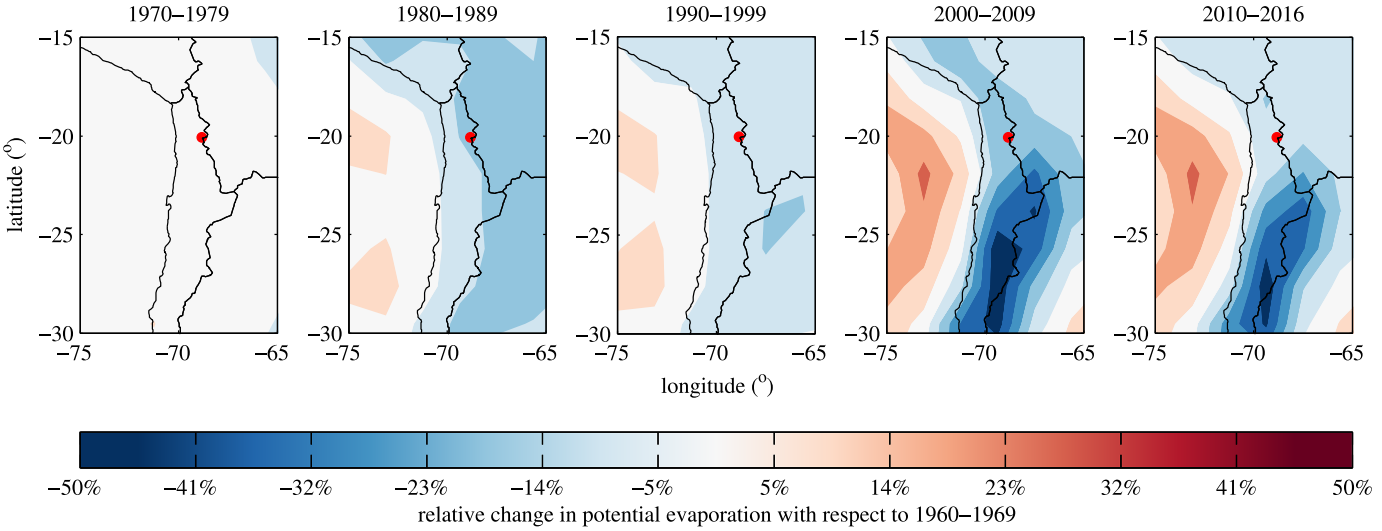

Figure 8. Frames of relative changes in the decadal average of the potential evaporation with respect to the 1960–1969 period. The red dot indicates the location of the study site.

of the twentieth century. These relative changes reached values up to −40% in the southern part of the altiplano.

4. Discussion

A spectral model specifically designed for long-term global climate change simulations of the thermodynamics and potential evaporation of shallow wetlands was presented. The primary variables computed by this model were the water and sediment temperature and the potential evaporation rates, which, in the context of Salars, closed the hydrological cycle [*de la Fuente and Niño*, 2010].

The spectral model solves the coupled system of heat conservation equations in the water column and the sediments, which is required because of the heat-reservoir role of the sediments in the heat budget of Salars [*de la Fuente and Niño*, 2010; *de la Fuente*, 2014a]. The standard method for simulating this heat-reservoir effect, referred here as the time-marching model, is not useful for solving the simulation spanning a period of 57 years shown in Figure 6. As a reference, in a computational domain of 2 m sediments, 1 month of simulation takes 1 day, which means that the simulation presented in Figure 6 would take approximately 1 year, whereas the spectral model only took less than 2 min for solution. This important reduction in the computational time is possible because the spectral model adopts the analytic solution of the second problem of Stockes for the sediments, which removes from the problem the solution of the heat diffusion equation in the sediments, yielding a computational domain whose extension should be proportional to the length scale α_n^{-1} [*Batchelor*, 1967; *White*, 2006].

In this article, we used the spectral model to study changes in the evaporation, and we used long-term records of daily evaporation rates measured in the Salar del Huasco catchment. The model was able to reproduce both seasonal cycles (Figure 5b) and climatic trends (Figure 7) in daily evaporations. It is important to note here that because of the lack of observations, the accuracy of NCEP-NCAR reanalysis before 1970 is not particularly good in the Southern Hemisphere [*Kistler et al*., 2001; *Tennant*, 2004]. However, it is also important to note that meteorological conditions are the boundary conditions of the spectral model, such that the accuracy of the results of the spectral model also depends on the accuracy of the meteorological forcing.

From a computational point of view, the ability of the spectral model to conduct long-term simulation in a couple of minutes relies on the linear decomposition of T_W and T_{WSI} of equations (6) and (9) and the use of the analytic solution of the second problem of Stokes for the sediment temperature. However, these simplifications mean that the parameters of the model (h, $(\rho c_p)_s$, $(\rho c_p)_w$, k_s, k_t^*) should be constant in time. Based on the results presented in this article, it is possible to argue that, as a first attempt, it is a reasonably good approximation in the context of the advantages that it implies. The surface albedo of the wetland was also assumed to be constant, and it was one of the calibrated parameters. However, the use of a constant value for the albedo is not a requirement of the spectral model presented here, and it was calibrated because the model results are very sensible on this parameter. Here it is important to highlight *Mendoza et al*. [2015] comment, who pointed out to the fact that several process-base models assume as constant several uncertain parameters whose value may have large impact on the accuracy and performance of the model. As we showed here, the surface albedo of the wetland is one of these parameters. In this sense, it is important to also highlight that sensitivity analyses are in general possible under the framework imposed by the computational constraints of the model (time and resources). Consequently, fast and accurate algorithms that deal with specific aspects of complex hydrological or ecological systems open the door for conducting more complex analyses for quantifying the uncertainty of the model results and the role that have the value of uncertain parameters on the model results.

In this article, we have assumed that all of the short-wave solar radiation that is not reflected back to the atmosphere is retained in the water column. This assumption is supported by previous results of *de la Fuente* [2014a]; however, it is unclear whether it is a reasonable assumption for very shallow water columns, where most of the downward solar radiation should be retained in the sediments rather than in the shallow water column. As a first approximation, it is possible to argue that this heat pathway in very shallow water column is represented by the spectral model presented here, as very shallow water columns would tend to heat more than deeper water column, and that increase in water temperature will increase heat diffusion

toward the sediments. However, the role of h on the way in which the solar radiation is absorbed by the water column or the sediments requires further analyses.

Long-term simulation of thermodynamics and potential evaporation of altiplanic wetlands revealed important changes in the potential evaporation in the system. In particular, potential evaporation has reduced in Salar del Huasco by 10%–20% with respect to the simulated rates during the second half of the twentieth century (Figure 6), which is explained by a reduction in the magnitude of the zonal wind. Furthermore, these trends are observed in the entire altiplano region, as shown in Figure 8. In particular, in the southern part of the altiplano region, the average potential evaporation in the last decade is 35% smaller than the average simulated rates for the 1960–1969 period. This climatic trend is clearly observed in the pan evaporation record that covers the period of 1964–2012.

In the context of closed endorreic basins of the altiplanic region, changes in potential evaporation are as important as changes in the precipitation. This is because the hydrological cycle is closed by evaporation, such that the total amount of water precipitated in the basin either locally evaporates in the basin or infiltrates toward the aquifer and then upwells in the perimeter of the Salar where it is completely evaporated [*Risacher et al*., 2003; *de la Fuente and Niño*, 2010]. Instantaneous evaporation in the basin is proportional to the potential evaporation, and it can be as large as 90% of the precipitated water [*Vega*, 2016], whereas the total evaporated water from the Salar can also be written as proportional to the potential evaporation [*Hornberger et al*., 2014]. The proportional constant for computing total evaporation from the Salar is given, among others, by the size of the shallow wetland and its salinity [*de la Fuente and Niño*, 2010], the ground water depth, and the soil salinity and humidity [*Nachshon et al*., 2011; *Aminzadeh et al*., 2016; *Hernández-López et al*., 2016]. In this manner, the reduction in the potential evaporation may imply that less water is evaporated in the basin, thus increasing the upwelled flow in the perimeter of the Salar or increasing the size of the lagoon and the elevation of the ground water depth. This preliminarily description does not consider the effect of changes in precipitation; thus, further studies are required for this aim.

5. Conclusion

Long-term prediction of the fate of aquatic ecosystems imposes computational constraints that, in some cases, make it impossible to find a solution. Consequently, numerical models for long-term simulations are required, and the spectral model presented in this article is a suitable tool for this purpose in shallow wetlands whose thermodynamics processes are modulated by both the atmosphere and the bottom sediments. The spectral model presented in this article has four important features that are highlighted: (i) it considers heat exchanges between the water and the sediments; (ii) it is able to naturally address the transition of $h \rightarrow 0$ (notice that the calibrated h in Table 3 are smaller than 1 mm); (iii) it is expressed in a spectral form that allows for use of the analytic solution of the second problem of Stokes for the sediment temperature, which reduces the computational requirements for solving the problem; and finally, (iv) it is a physical-based model with parameters that have physical meaning (water depth, albedo, heat capacity, and conductivity) and characterize the local properties of the study site.

We used the spectral model for computing evaporation in Salar del Huasco; however, it is important to notice that as long as meteorological information is available, the spectral model can be used in other locations, with or without a shallow water column.

Appendix A: Matlab Routine for Computing Water Temperature With Spectral Model

```
function [Tw,diffTw]=calcTw(t,Ta,q,P,Uw,Hsw,CC,Zwnd,ZTa);
%
% Matlab routine for computing water temperature in shallow wetland
% de la Fuente and Meruane [2017], WRR, doi:
%
% [Tw,diffTw]=calcTw(t,Ta,q,P,U10,Hsw,CC,Zwnd,ZTa);
% t: time in days
% Ta: Air temperature in [^oC] measured at ZTa [m] above the water surface
```

```
% q: air mixing ration [gr/gr] measured at ZTa [m] above the water surface
% P: atmospheric pressure [Pa]
% Uw: Wind speed [m/s] measured at Zwnd [m] above the water surface
% Hsw: Incident short-wave solar radiation [W/m^2]
% CC: Cloud cover [-]
% Zwnd: Elevation of wind speed above the water surface [m]
% Zwnd: Elevation of air temperature and mixing ration above the water surface [m]
%
% This routine considers that exist the following subroutines that are specified by the user
% load_modelparams: Load model parameters, and provides one single value of the following parameters:
%    beta_H: linearization of H, recommended=20W/m^2/^oC
%    rhocpw: heat capacity of water [J/m^3/^oC].
%    rhocps: heat capacity of th sediments [J/m^3/^oC].
%    ks: Heat diffusion coefficient in the sediments [m^2/s].
%    h: Water depth [m].
% load_molPropWater: Load characteristic values for molecular properties of water
%    nu: water viscosity [m^2/s];
%    rho_w: Water density [kg/m^3]
%    beta: thermal expansion coefficient [m^2/s];
%    Pr: Prandtl number [-];
% calcKt: Provides one single value for the heat transfer [m/s] velocity at the sediment-
% water interface
%    It uses as argument the Grashof and the bottom shear velocity computed by assuming
% a Couette Flow
% [H,ustar,Hlw_in,Hlw_ou,Hsw,Hc,He,rho_a]=calcH(Hsw,P,Uw,Ta,Tw,q,CC,Zwnd,ZTa);
%    Routine that computes H as a function of meteorological variables
%    Hsw,P,Uw,Ta,q,CC,Zwnd,ZTa, and the water temperature Tw.
%    Here the heat flux exchanged with the atmosphere is defined following the sign
%    convection of the manuscript, where H is positive if it flows from the wetland to the
%    atmosphere.
% calcH function used here also provides the
%    ustar: Wind shear velocity = sqrt(tau/rho_a)
%    Hlw_in: Incident long-wave radiation
%    Hlw_ou: Emitted long-wave radiation
%    NHsw: Net short-wave radiation (incident - reflected
%    Hc: Sensible heat flux
%    He: Latent heat flux
%    rho_a: Air density

[beta_H,rhocpw,rhocps,ks,h]=load_modelparams;
[nu,rho_w,beta,Pr]=load_molPropWater;
kappa=nu/Pr; % heat diffusion coefficient in the water

dt=(t(2)-t(1))*86400; % time step
Fs=1/(dt); % Sampling frequency
r=0.7; % Underrelaxation underrelaxation factor equation (25)

N = floor(length(Uw)/2); % Computes the limits of the Fourier decomposition equation (6)

omega = 2*pi*Fs/(2*N)*(-N:N)'; %frequency vector

maxitera=50; %maximum number of iterations

% Starting water temperature for the iteration
```

```
Twsim=zeros(length(Uw),1)+10;
Tw=Twsim;
Tssim=Tw;
Twsim=Tw;

% it is called here to obtain the air density and wind shear speed
[H,ustar,Hlw_in,Hlw_ou,NHsw,Hc,He,rho_a]=calcH(Hsw,P,Uw,Ta,Tw,q,CC,Zwnd,ZTa);

% The bottom shear velocity ustar_b is required in equation (23), and estimated considering a Couette flow
ustar_b=sqrt(rho_a./rho_w).*ustar;

% Definition of characteristic kt* required equation (12)
Ra=max(Tssim-Twsim,0)*beta*9.81/(nu)^2*Pr*h^3;
kt=calcKt(Ra,ustar_b);
K=kt*rhocpw;

% Main loop
itera=0;
while (itera<maxitera)
itera=itera+1;

% Step 1
[H,ustar,Hlw_in,Hlw_ou,NHsw,Hc,He,rho_a]=calcH(Hsw,P,Uw,Ta,Tw,q,CC,Zwnd,ZTa,albedo);
H=H-beta_H*Tw;
O=1i*omega*rhocph;
D=sqrt(abs(omega)/2/ks).*ks*rhocps.*(1+sign(omega)*1i);

% Step 2
Y = fftshift(fft(H));

% Step 3 for h=0
if h==0
   ts=-Y/(2*N+1)./(D+beta_H);
End

% Step 3 for h>0
if h>0
   ts=-Y/(2*N+1)./(O+KT*(1-KT./(KT+D))+beta_H);
   tss=ts.*KT./(KT+D);
   Tssim=((ifft(ifftshift(tss))))*(2*N+1);
End

% Step 4
Twsim=((ifft(ifftshift(ts))))*(2*N+1);
Two=Tw;
Tw = (1-r)*Twsim+r*Tw;

% Step 5
if h>0
   Ra=max(Tssim-Twsim,0)*beta*9.81/(nu)^2*Pr*h^3;
   kt=calcKt(Ra,ustar_b);
   K=kt*rhocpw;
End
```

```
    % Step 6
    difTw(itera)=std((Tw-Two));
End
```

Acknowledgments
This study was financed by the Fondecyt project 1140821. We thank V. Molina and C. Dorador for the meteorological data measured in Salar del Huasco. Data used in this manuscript can be downloaded from MODIS Land surface temperature: https://lpdaac.usgs.gov/dataset_discovery/modis/modis_products_table/mod11a1_v006; NCEP-NCAR atmospheric reanalysis: https://www.esrl.noaa.gov/psd/data/gridded/data.ncep.reanalysis.surface.html, Meteorological information between September 2016 and December 2016: http://www.ceazamet.cl/; Air temperature in 1981 and 1982, and pan evaporations between 1964 and 2012: https://siac.mop.gov.cl/Atencion/ingresoCiudadano.do, indicating "Dirección General de Aguas" alternative in the "A quién dirige su Consulta" field of the form (to whom), and "Región de Tarapacá" alternative in the "A qué región asocia su Consulta" field of the form (which region).

References

Adrian, R., et al. (2009), Lakes as sentinels of climate change, *Limnol. Oceanogr.*, *54*, 2283–2297, doi:10.4319/lo.2009.54.6_part_2.2283.
Aminzadeh, M., M. L. Roderick, and D. Or (2016), A generalized complementary relationship between actual and potential evaporation defined by a reference surface temperature, *Water Resour. Res.*, *52*, 385–406, doi:10.1002/2015WR017969.
Arias, E. D. C., and C. Farfán (1997), Hydrobiology of a salt pan from the Peninsula of Baja California, Mexico, *Int. J. Salt Lake Res.*, *6*, 233–248, doi:10.1023/A:1009051919908.
Batchelor, G. K. (1967), *An Introduction to Fluid Dynamics*, Cambridge Univ. Press.
Belluscio, A. (2009), High window on the past [online], *Nat. News*, doi:10.1038/news.2009.924.
Bogan, T., O. Mohsemi, and H. G. Stefan (2003), Stream temperature-equilibrium temperature relationship, *Water Resour. Res.*, *39*(9), 1243, doi:10.1029/2003WR002034.
Cabrol, N. A., et al. (2009), The High-Lakes Project, *J. Geophys. Res.*, *114*, G00D06, doi:10.1029/2008JG000818.
Cerco, C. F., and S. P. Seitzinger (1997), Measured and modeled effects of benthic algae on eutrophication in Indian River-Rehoboth Bay, Delaware, *Estuaries*, *20*, 231, doi:10.2307/1352733.
Confalonieri, R., L. Mariani, and S. Bocchi (2005), Analysis and modelling of water and near water temperatures in flooded rice (*Oryza sativa* L.), *Ecol. Modell.*, *183*, 269–280, doi:10.1016/j.ecolmodel.2004.07.031.
Dade, W. B. (1993), Near-bed turbulence and hydrodynamic control of diffusional mass transfer at the sea floor, *Limnol. Oceangr.*, *38*, 52–69.
de la Fuente, A. (2014a), Heat and dissolved oxygen exchanges between the sediment and water column in a shallow salty lagoon, *J. Geophys. Res. Biogeosci.*, *119*, 596–613, doi:10.1002/2013JG002413.
de la Fuente, A. (2014b), Methodology for analyzing dissolved oxygen consumption in benthic chambers, *J. Environ. Eng.*, *141*, 4014098, doi:10.1061/(ASCE)EE.1943-7870.0000926.
de la Fuente, A., and C. Meruane (2017), Dimensionless numbers for classifying the thermodynamics regimes that determine water temperature in shallow lakes and wetlands, *Environ. Fluid Mech.*, 1–18, doi:10.1007/s10652-017-9536-x, in press.
de la Fuente, A., and Y. Niño (2010), Temporal and spatial features of the thermohydrodynamics of shallow salty lagoons in northern Chile, *Limnol. Oceanogr.*, *55*, 279–288, doi:10.4319/lo.2010.55.1.0279.
de la Fuente, A., C. Ordóñez, and R. Pérez (2016), Diffusional mass transfer coefficient at the water-sediment interface for wind-induced flow in very shallow lagoons, *Environ. Fluid Mech.*, *16*, 539–558, doi:10.1007/s10652-015-9437-9.
Dorador, C., D. Meneses, V. Urtuvia, C. Demergasso, I. Vila, K.-P. Witzel, and J. F. Imhoff (2009), Diversity of *Bacteroidetes* in high-altitude saline evaporitic basins in northern Chile, *J. Geophys. Res.*, *114*, G00D05, doi:10.1029/2008JG000837.
Dorador, C., I. Vila, F. Remonsellez, J. F. Imhoff, and K.-P. Witzel (2010), Unique clusters of Archaea in Salar de Huasco, an athalassohaline evaporitic basin of the Chilean Altiplano, *FEMS Microbiol. Ecol.*, *73*, 291–302.
Fang, X., and H. G. Stefan (1998), Temperature variability in lake sediments, *Water Resour. Res.*, *34*, 717–729.
Garratt, J. R. (1992), *The Atmospheric Boundary Layer*, Cambridge Univ. Press, Cambridge, U. K.
Golosov, S., and G. Kirillin (2010), A parameterized model of heat storage by lake sediments, *Environ. Modell. Software*, *25*, 793–801, doi:10.1016/j.envsoft.2010.01.002.
Hernández, K. L., B. Yannicelli, L. M. Olsen, C. Dorador, E. J. Menschel, V. Molina, F. Remonsellez, M. B. Hengst, and W. H. Jeffrey (2016), Microbial activity response to solar radiation across contrasting environmental conditions in Salar de Huasco, Northern Chilean Altiplano, *Front. Microbiol.*, *7*, 1857, doi:10.3389/fmicb.2016.01857.
Hernández-López, M. F., I. Braud, J. Gironás, F. Suárez, and J. F. Muñoz (2016), Modelling evaporation processes in soils from the Huasco salt flat basin, Chile, *Hydrol. Processes*, *30*, 4704–4719, doi:10.1002/hyp.10987.
Herrera, V., I. de Gragori, and H. Pinochet (2009), Assessment of trace elements and mobility of arsenic and manganese in lagoon sediments of the Huasco and Coposa salt flats, Chilean Altiplano, *J. Chil. Chem. Soc.*, *54*, 454–459, doi:10.4067/S0717-97072009000400029.
Hondzo, M., T. Feyaerts, R. Donovan, and B. L. O'Connor (2005), Universal scaling of dissolved oxygen distribution at the sediment-water interface: A power law, *Limnol. Oceangr.*, *50*, 1667–1676.
Hornberger, G. M., P. L. Wiberg, J. P. Raffensperger, and P. D'Odorico (2014), *Elements of Physical Hydrology*, Johns Hopkins Univ. Press, Baltimore, Md.
Hussaini, M. Y., and T. A. Zang (1987), Spectral methods in fluid dynamics, *Annu. Rev. Fluid Mech.*, *19*, 339–367, doi:10.1146/annurev.fl.19.010187.002011.
Imberger, J. (2013), *Environmental Fluid Dynamics: Flow Processes, Scaling, Equations of Motion, and Solutions to Environmental Flows*, Academic, Oxford, U. K.
Jimenez, I. M., M. Kühl, A. W. D. Larkum, and P. J. Ralph (2008), Heat budget and thermal microenvironment of shallow-water corals: Do massive corals get warmer than branching corals?, *Limnol. Oceanogr.*, *53*, 1548–1561, doi:10.4319/lo.2008.53.4.1548.
Jørgensen, S., and G. Bendoricchio (2001), *Fundamentals of Ecological Modelling*, Elsevier Sci., Amsterdam.
Junk, W. J., S. An, C. M. Finlayson, B. Gopal, J. Květ, S. A. Mitchell, W. J. Mitsch, and R. D. Robarts (2013), Current state of knowledge regarding the world's wetlands and their future under global climate change: A synthesis, *Aquat. Sci.*, *75*, 151–167, doi:10.1007/s00027-012-0278-z.
Kalnay, E., et al. (1996), The NCEP/NCAR 40-Year Reanalysis Project, *Bull. Am. Meteorol. Soc.*, *77*, 437–471.
Kistler, R., et al. (2001), The NCEP-NCAR 50-year reanalysis: Monthly means CD-ROM and documentation, *Bull. Am. Meteorol. Soc.*, *82*, 247–267, doi:10.1175/1520-0477(2001)082<0247:TNNYRM>2.3.CO;2.
Kuwagata, T., T. Hamasaki, and T. Watanabe (2008), Modeling water temperature in a rice paddy for agro-environmental research, *Agric. For. Meteorol.*, *148*, 1754–1766, doi:10.1016/j.agrformet.2008.06.011.
Le, P. M., and D. V. Papavassiliou (2006), Turbulent heat transfer in plane Couette flow, *J. Heat Transfer*, *128*, 53, doi:10.1115/1.2130404.
Liang, X., E. F. Wood, and D. P. Lettenmaier (1999), Modeling ground heat flux in land surface parameterization schemes, *J. Geophys. Res.*, *104*, 9581–9600, doi:10.1029/98JD02307.

López-González, P. J., F. Guerrero, and M. Carmen Castro (1997), Seasonal fluctuations in the plankton community in a hypersaline temporary lake (Honda, southern Spain), *Int. J. Salt Lake Res.*, *6*, 353–371, doi:10.1007/BF02447916.
Martynenko, O. G., and P. P. Khramtsov (2005), *Free-Convective Heat Transfer: With Many Photographs of Flows and Heat Exchange*, Springer, Berlin.
McCabe, R. M., P. Estrade, J. H. Middleton, W. K. Melville, M. Roughan, and L. Lenain (2010), Temperature variability in a shallow, tidally isolated coral reef lagoon, *J. Geophys. Res.*, *115*, C12011, doi:10.1029/2009JC006023.
McJannet, D., F. Cook, R. McGloin, H. McGowan, S. Burn, and B. Sherman (2013), Long-term energy flux measurements over an irrigation water storage using scintillometry, *Agric. For. Meteorol.*, *168*, 93–107, doi:10.1016/j.agrformet.2012.08.013.
Mendoza, P. A., M. P. Clark, M. Barlage, B. Rajagopalan, L. Samaniego, G. Abramowitz, and H. Gupta (2015), Are we unnecessarily constraining the agility of complex process-based models?, *Water Resour. Res.*, *51*, 716–728, doi:10.1002/2014WR015820.
Mertins, A. (1999), *Signal Analysis: Wavelets, Filter Banks, Time-Frequency Transforms, and Applications*, John Wiley, Chichester, U. K.
Moss, R. H., et al. (2010), The next generation of scenarios for climate change research and assessment, *Nature*, *463*, 747–756, doi:10.1038/nature08823.
Nachshon, U., N. Weisbrod, M. I. Dragila, and A. Grader (2011), Combined evaporation and salt precipitation in homogeneous and heterogeneous porous media, *Water Resour. Res.*, *47*, W03513, doi:10.1029/2010WR009677.
Necati, O. (1977), *Basic Heat Transfer*, McGraw-Hill, New York.
O'Connor, B. L., and M. Hondzo (2008), Dissolved oxygen transfer to sediments by sweep and eject motion in aquatic environments, *Limnol. Oceangr.*, *53*, 578–599.
Paraska, D. W., M. R. Hipsey, and S. U. Salmon (2014), Sediment diagenesis models: Review of approaches, challenges and opportunities, *Environ. Modell. Software*, *61*, 297–325, doi:10.1016/j.envsoft.2014.05.011.
Patankar, S. (1980), *Numerical Heath Transfer and Fluid Flow*, Hemisphere, Washington, D. C.
Piccolo, M. C. (2009), Heat energy in coastal wetlands, in *Coastal Wetlands: An Integrated Ecosystem Approach*, edited by G. M. E. Perillo et al., pp. 211–230, Elsevier, Hoboken, N. J.
Prats, J., A. Ramos, J. Armengol, and J. Dolz (2011), Comparison of models for calculation of Diel sediment-water heat flux from water temperatures, *J. Hydraul. Eng.*, *137*, 1135–1147, doi:10.1061/(ASCE)HY.1943-7900.0000434.
Risacher, F., H. Alonso, and C. Salazar (2003), The origin of brines and salts in Chilean salars: A hydrochemical review, *Earth Sci. Rev.*, *63*, 249–293.
Seber, G. A. F., and C. J. Wild (2003), *Nonlinear Regression*, John Wiley, Chichester, U. K.
Sheng, J., J. P. Wilson, and S. Lee (2009), Comparison of land surface temperature (LST) modeled with a spatially-distributed solar radiation model (SRAD) and remote sensing data, *Environ. Modell. Software*, *24*, 436–443, doi:10.1016/j.envsoft.2008.09.003.
Smesrud, J. K., M. S. Boyd, R. H. Cuenca, and S. L. Eisner (2014), A mechanistic energy balance model for predicting water temperature in surface flow wetlands, *Ecol. Eng.*, *67*, 11–24, doi:10.1016/j.ecoleng.2014.03.006.
Smith, N. P. (2002), Observations and simulations of water-sediment heat exchange in a shallow coastal lagoon, *Estuaries*, *25*, 483–487, doi:10.1007/BF02695989.
Stull, R. B. (1988), *An Introduction to Boundary Layer Meteorology*, Springer Netherlands.
Tennant, W. (2004), Considerations when using pre-1979 NCEP/NCAR reanalyses in the southern hemisphere, *Geophys. Res. Lett.*, *31*, L11112, doi:10.1029/2004GL019751.
Timms, B. V. (2005), Salt Lakes in Australia: Present problems and prognosis for the future, *Hydrobiologia*, *552*, 1–15, doi:10.1007/s10750-005-1501-x.
van Vuuren, D. P., et al. (2011), The representative concentration pathways: An overview, *Clim. Change*, *109*, 5–31.
Vega, A. (2016), *Balance hídrico de la cuen-ca del Salar del Huasco mediante el modelo hidrológico de simulación TOPMODEL usando información del reanálisis atmósferico*, Mem. para optar al título de Ing. Civ., Univ. de Chile, Santiago.
Versteeg, H. K., and W. Malalasekera (1995), *An Introduction to Computational Fluid Dynamics. The Finite Volume Methods*, Longman Group Ltd, U. K.
Wan, Z. S. H., and G. Hulley (2015), *MOD11A1 MODIS/Terra Land Surface Temperature/Emissivity Daily L3 Global 1 km SIN Grid V006*, NASA EOSDIS Land Process. DAAC.
White, F. M. (2006), *Viscous Fluid Flow*, McGraw-Hill, New York.
Williamson, C. E., J. E. Saros, W. F. Vincent, and J. P. Smol (2009), Lakes and reservoirs as sentinels, integrators, and regulators of climate change, *Limnol. Oceanogr.*, *54*, 2273–2282, doi:10.4319/lo.2009.54.6_part_2.2273.
Willmott, C. J. (1981), On the validation of models, *Phys. Geogr.*, *2*, 184–194, doi:10.1080/02723646.1981.10642213.